AD-A084 967 STEVENS INST OF TECH HOBOKEN NJ DEPT OF PHYSICS F/G 20/8
STUDY OF THE ANATOMY OF THE X-RAY AND NEUTRON PRODUCTION SCALIN--ETC(U)
NOV 79 V NARDI, W H BOSTICK, W PRIOR AFOSR-75-2754
UNCLASSIFIED SIT-P2002-1179 AFOSR -TR-80-0411 NL

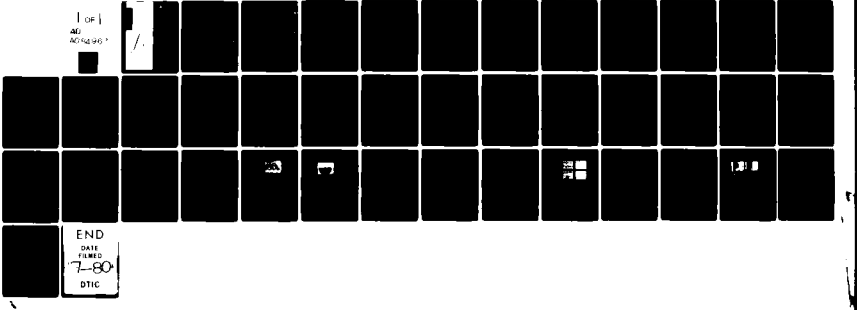

END
DATE FILMED
7-80
DTIC

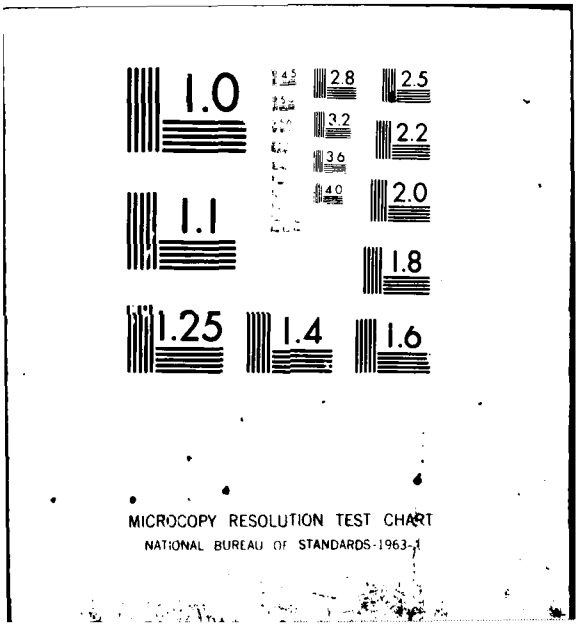
1.0
2.8
2.5
3.2
2.2
3.6
4.0
2.0
1.1
1.8
1.25
1.4
1.6
MICROCOPY RESOLUTION TEST CHART
NATIONAL BUREAU OF STANDARDS-1963-A

SIT-P2002-1179

DEPARTMENT OF PHYSICS

Study of the Anatomy of the X-Ray and Neutron Production Scaling Laws in the Plasma Focus

V. Nardi, W. H. Bostick, W. Prior

Final Report AFOSR Grant 75-2754
Period Oct. 1, 1978 - Sept. 30, 1979

November 1979

STEVENS INSTITUTE OF TECHNOLOGY

CASTLE POINT STATION
HOBOKEN, NEW JERSEY 07030

SECURITY CLASSIFICATION OF THIS PAGE (When Data Entered) Unclassified

REPORT DOCUMENTATION PAGE

READ INSTRUCTIONS BEFORE COMPLETING FORM

1. REPORT NUMBER: AFOSR-TR-80-0411	2. GOVT ACCESSION NO.: AD A084967
3. RECIPIENT'S CATALOG NUMBER:	
4. TITLE (and Subtitle): STUDY OF THE ANATOMY OF THE X-RAY AND NEUTRON PRODUCTION SCALING LAWS IN THE PLASMA FOCUS (PARTICLE ENERGY SPECTRUM AND OPTIMIZATION CRITERIA).	5. TYPE OF REPORT & PERIOD COVERED: Final Technical Report Ending September 30, 1979
	6. PERFORMING ORG. REPORT NUMBER: SIT-P2002-1179
7. AUTHOR(s): V. Nardi, W. H. Bostick, W. Prior	8. CONTRACT OR GRANT NUMBER(s): AFOSR-75-2754
9. PERFORMING ORGANIZATION NAME AND ADDRESS: Stevens Institute of Technology, Physics/Engineering Physics Department, Castle Point Station, Hoboken, New Jersey 07030	10. PROGRAM ELEMENT, PROJECT, TASK AREA & WORK UNIT NUMBERS: 61102F 2301 A2
11. CONTROLLING OFFICE NAME AND ADDRESS: Department of the Air Force, Air Force Office of Scientific Res., Directorate of Physics, Bldg. 410 Bolling Air Force Base, DC 20332	12. REPORT DATE: November 1979
	13. NUMBER OF PAGES: 24 + 15
14. MONITORING AGENCY NAME & ADDRESS (if different from Controlling Office): 12 41	15. SECURITY CLASS. (of this report): unclassified
	15a. DECLASSIFICATION/DOWNGRADING SCHEDULE

16. DISTRIBUTION STATEMENT (of this Report)

Approved for public release; distribution unlimited.

17. DISTRIBUTION STATEMENT (of the abstract entered in Block 20, if different from Report)

9 Final technical rept. 1 Oct 78-30 Sep 79

18. SUPPLEMENTARY NOTES

To be published with variation and with additional material in "Proceedings of the Second International Conference on Megagauss Magnetic Field Generation" 29 May - 1 June 1979, Washington, D. C., P. Turchi (Naval Research Laboratory) edit.

19. KEY WORDS (Continue on reverse side if necessary and identify by block number)

Neutron yield, x-ray emission, electron beams, ion beams, energy spectrum, scaling laws for plasma focus, optimization criteria, terawatt ions and electron beams, correlation coefficients, beam-induced damage, high-intensity ion and electron beams, dendrites, plasma focus.

20. ABSTRACT (Continue on reverse side if necessary and identify by block number)

Optimum conditons for plasma focus operations have been experimentally analyzed in terms of (A) The fine structure of the axial-current channel during maximum of compression. (B) Correlation coefficient, for neutron yield n (by D_2 discharges) and the multiplicity of the electron beam pulses; (C) Different values of the electrode voltage. The current distribution near the axial plasma column during the explosive decay of the column has been monitored and correlated with the electron beam production. Plasma

DD FORM 1 JAN 73 1473 EDITION OF 1 NOV 65 IS OBSOLETE 334590 UNCLASSIFIED

SECURITY CLASSIFICATION OF THIS PAGE (When Data Entered)

focus discharges by our mode of operation generate high-intensity deuteron beams ($\sim 10^5$ Amp) with a $\gtrsim$ 300-keV-peaked spectrum and electron beams, with an energy distribution similarly peaked at 300-400 keV. The energy spectrum is determined by two independent methods (time of flight and target-damage data). The spectrum varies from shot to shot but the main features are observed in all discharges. In each discharge we observe on a time interval of 100-300 nanosec a sequence of beam pulses (1-10), with the same multiplicity of the peak in the rate of change $|dI/dt|$ of the electrode current I. The filamentary structure of the electron beam and the internal structure of the filament have been analyzed with a space resolution better than $\sim$ 1 μm.

Final Scientific Report on AFOSR Grant 75-2754 for Period Ending September 30, 1979

STUDY OF THE ANATOMY OF THE X-RAY AND NEUTRON PRODUCTION SCALING LAWS IN THE PLASMA FOCUS (PARTICLE ENERGY SPECTRUM AND OPTIMIZATION CRITERIA)

V. Nardi, W. H. Bostick, W. Prior

Optimum conditions for plasma focus operations have been experimentally analyzed in terms of (A) The fine structure of the axial-current channel during maximum of compression. (B) Correlation coefficient, for neutron yield n (by D_2 discharges) and the multiplicity of the electron beam pulses; (C) Different values of the electrode voltage. The current distribution near the axial plasma column during the explosive decay of the column has been monitored and correlated with the electron beam production. Plasma focus discharges by our mode of operation generate high-intensity deuteron beams ($\sim 10^5$ Amp) with a 300-keV-peaked spectrum and electron beams, with an energy distribution similarly peaked at 300-400 keV. The energy spectrum is determined by two independent methods (time of flight and target-damage data). The spectrum varies from shot to shot but the main features are observed in all discharges. In each discharge we observe on a time interval of 100-300 hanosec a sequence of beam pulses (1-10),with the same multiplicity of the peak in the rate of change |dI/dt| of the electrode current I. The filamentary structure of the electron beam and the internal structure of the filament have been analyzed with a space resolution better than ~ 1 μm.

1. Introduction

Empirical scaling laws[1] as $n = AE^{\alpha}$ $(1.5 \leqq \alpha \leqq 2.2)$, $n = BI^{\beta}$ $(3.3 \leqq \beta \leqq 5)$ are frequently used to correlate the radiated energy with macroscopic parameters in a plasma focus system (n = D-D neutrons/shot in D_2 discharges. the emitted x-ray energy could also be used instead of n for different values for α, β, A, B; E = capacitor bank energy at maximum voltage V, I = peak value of the current on the electrodes); the plasma focus is considered to operate by optimum conditions e.g. by the choice of electrode radii and D_2 - pressure p in the discharge chamber which give the maximum n for a fixed value of $E = \frac{1}{2} cv^2$. By a detailed analysis of the fine structure of the axial-current channel (pinch stage) in the plasma focus we can gain insight in the mechanisms by which densification of energy in space and time is achieved. A correlation is found among typical parameters of the fine structure (as the multiplicity of localized sources of x-rays and of electron-beam pulses) and the neutron yield n. This type of information is complementing the usual scaling laws and becomes particularly useful to understand the limits of validity of the scaling laws and what may cause their failure. A frequent cause of this failure is a too high speed of the current sheath in the interelectrodegap, a too thick current sheath or restrike and formation of a second current sheath behind the first-formed current sheath. These conditions affect also the fine structure of the plasma focus as it is observed during and after the explosive phase of the axial current channel. The correlation coefficients for n and multiplicity of electron-beam pulses have been experimentally determined and are presented in Ref. 2 (attached to this report). Method of observation of the electron beam pulses and the typical energy spectrum of the ion beam (which is produced at the same time and by the same localized source of the electron beam) are also presented in

Ref. 1. The rate of change $|dI/dt|$ the electrode current I during the explosive phase of the pinch has a critial role in determining the yield n and is related to the formation of current loops in the region of space near the axial current channel. A detailed description of the role of these loops is presented in Section 3 of this report.

The current pattern with a multiplicity of current loops in the axial region of a plasma focus discharge is determined by x-ray intensity and intensity anisotropy measurements. A current loop configuration which is consistent with the x-ray data fits the time-resolved image (5 ns exposure by visible light) of the discharge region with a particle density $\sim 10^{19}$ cm^{-3}. The amperian current in a localized loop (loop diameter $\lesssim$ 1-3 mm) can become higher by a factor > 3 than the total current ($\sim$ 0.7 MA) on the electrodes and can generate a peak field intensity $\sim 10^{8}$ G. A space resolution $\sim$ 10 μm and $\sim$ 0.1 mm of the plasma structure is obtained respectively by microdensitometer scanning of photographs from x-ray pinhole cameras and visible-light image-converter photographs Ions and electron beam ($\sim$ 10 keV - 3 MeV, beam power $\sim$ TW/cm^2, 1 - 10 ns) are generated by the field decay on a ns time scale.

Ref. 1. Zucker, O., Bostick, W., Long, J., Luce, J., Shalin, H., Nucl. Instrum. Methods 145 (1977) 185.

Ref. 2. V. Nardi, W. H. Bostick, J. Feugeas, W. Prior, C. Cortese, Proc. IAEA Int. Conference on Plasma Physics and Controlled Nuclear Fusion Research, Innsbruck, 23-30 Aug. 1978, Vol. II, P.

2. Publications

During the period October 1, 1978 - September 30, 1979 one full-length paper has been completed, "Megagauss Fields and Current Pattern in Focussed Discharges", W. H. Bostick, V. Nardi, J. Feugeas, W. Prior, Proc. Second International Conference on Megagauss Magnetic Field Generation, 29 May - 1 June 1979, Washington, D. C., P. Turchi (NRL) edit. and two other papers have been submitted for publication; the abstracts of three papers have been published: Electron Beams from an Inductive Generator; W. H. Bostick, J. Feugeas, V. Nardi, C. Cortese, Bull. American Phys. Soc., vol. 24, p. 1008, Oct. 1, 1979, Internal Structure of Electron Beams; V. Nardi, W. H. Bostick, J. Geugeas, W. Prior, Bull. American Phys. Soc., vol. 24, p. 1013, Oct. 1, 1979 and Production of Plasmoids Emitting > 2.4 MeV Deuterons; W. H. Bostick, V. Nardi, W. Prior, Bull. American Phys. Soc., vol. 24, p. 1039, Oct. 1, 1979. Other papers have been published during the research period ending September 1978:

(1) Energy Spectra of Deuteron Beams and Electron Beams from Focused Discharges and Optimization Criteria, V. Nardi, W. H. Bostick, J. Feugeas, W. Prior, C. Cortese, Proc. IAEA Int. Conference on Plasma Physics and Controlled Nuclear Fusion Research, Innsbruck, 23-30 Aug. 1978, Vol. III; (2) Production of GW Electron and Ion Beams by Focused Discharges, W. H. Bostick, J. Feugeas, V. Nardi, W. Prior, C. Cortese, Proc. Energy Storage, Compression and Switching Int. Conf. (II), Venice, Dec. 5-8, 1978, Plenum Publ. New York; (3) Structure and Propagation of Electron Beams, V. Nardi, Proc. Energy Storage, Compression and Switching Int. Conf. 1978; (4) Collective Acceleration and Focussing of Fast Ion Bursts, J. Luce, W. H. Bostick, V. Nardi, Proc. Int. Conf. on Collective

Methods of Acceleration, Univ. of California, Irvine, May 22-25, 1978, Harwood Academic Publ., London, p. 423-507; (5) Electron Beams and 10^5 Amp Deuteron Beams by Focused Discharges, W. H. Bostick, V. Nardi, W. Prior, Optic. Soc. of Am., Tech. Digest, Feb. 1978, San Diego, p. Th 21-25.

3 . Current Pattern in Focussed Discharges

Plasma focus discharges in deuterium or hydrogen with a peak current $I_m \gtrsim 0.5 - 0.8$ MA and voltage 11 - 18 kV on the electrodes can generate a magnetic field intensity B with peak values $B_m \gtrsim 10^6 - 10^8$ G within cylindrical regions of diameter $\lesssim 4 - 0.1$ mm along the electrode axis.[1,2] Experimental determinations of B_m have been based so far on: (a) spectroscopic observations (splitting of impurity CV lines)[1]; (b) derivation of the electron current, i.e., mean velocity orientation, electron density and energy spectrum, respectively by the observed intensity anisotropy of the x-ray emission, by calibrating x-ray films and by differential window measurements from localized x-ray sources (diameter 0.1 - 1 mm) which fit in space and time the axial current peaks.[2] Method (a) has a space resolution of a few mm's and gives $B_m \lesssim 2 \times 10^6$ G. Method (b) has a maximum of space resolution ($\sim$ 0.1 mm) and gives $B_m \gtrsim 2 \times 10^8$ G on the surface of localized x-ray sources in the axial region. The building up of B_m can be related to the role that electrons and ions have as current carriers at different times and in different locations of the discharge. Intensity and multiplicity of the x-ray sources by pinhole photographs fit the corresponding time-resolved data (by scintillation detectors) of x-ray and of neutron emission pulses with a value of the correlation coefficient > 0.4 from 50 - 100 discharges.[3] The anisotropy of the 1 - 10 keV x-ray emission[2] (maximum of intensity $I_{90}o$ at 90^o with respect to the electrode axis) and of the neutron energy spectrum (the observed energy maximum in the direction of the electrode axis, E_0o , is higher by a factor $\cong 1.3$ than the maximum energy in the orthogonal direction)[4] is caused by the axial beam structure of the electron and ion flow within the localized sources.[2,5]

The amperian current of the electron beams ejected from the focus region can be measured by using a hollow center electrode (anode; diameter 3.4 cm) and a drift chamber (a pyrex pipe) attached to the rear end of the anode [6]; see Sect.3. Rogowski coils encircling the pyrex pipe give typical values of 1 - 10 kA for this electron beam current.(†) One beam with a composite structure is ejected for each of the peaks (1 - 5) of the $|dI/dt|$ signal vs. time from the total current $I(t)$ on the electrodes in a single discharge.[6] Ions and electron beams are also detected via beam damage on different type of targets at 0^0 (front) and 180^0 (rear) on the electrode axis. Our observations indicate that ions beams are ejected axially, mostly in the forward direction and, by a much smaller amount also in the direction of the anode. We look for suitable current patterns which are consistent with the observed ion and electron beam emission and with the building up of B_m.

2. Current loops.

By our mode of operation of the plasma focus the regions of maximum luminosity correspond also to regions of maximum current density.[7] Image converter photographs (visible light, 5 ns exposure) gives the profile of the axial column during the time of maximum I (at the end of the first quarter of discharge period $T \simeq 8.8$ μs) and within 50 ns from the time (t=0) of the peak in the $|dI/dt|$ signal (Fig. 1). The maximum B_m is also observed at this time.

(†) including "return" current.

The current flow has a density peak on the wall of the "hollow" axial column with a cusped profile and a typical diameter of about 4 mm. During the life-time of the axial plasma column (40 - 100 ns) secondary pinchings, i.e. neckings, develop over a time interval $\Delta t \gtrsim 5 - 10$ ns[8] which further reduce the column diameter to $\lesssim$ 1-2 mm in one location or at several locations along the electrode axis z (Fig. 1 b,d). At a low applied voltage (11 kV) on the electrodes the first $|dI/dt|$ peak may occur in our system also more than 20 - 40 ns after the column necking. This peak is related in time with the azimuthal tearing of the column wall in a 4-mm diameter region rather than with the column interruption at a necking point.[6] The image converter photographs agree with shadowgrams data[8] and indicate that dense plasma is flowing outward from the column cusps. The formation of current loops is suggested by the luminous pattern and by the signal from probes (circular loop diameter 2 mm) with three different orientations which give the components B_θ , B_z , B_r of the magnetic field as functions of time (Fig. 2,3,4) at different locations.

Specifically the presence of closed loops is suggested near the second necking (from right) of Fig. 1b, between third and fourth cusps (upper side) of Fig. 1c, fifth and sixth cusps of Fig. 1d, third and fifth cusps (upper side) of Fig. 2a, first and second (upper side) of Fig. 3a, fourth (upper side) of Fig. 4a, third and fourth cusps (lower side) of Fig. 4b. In Fig. 2c, 3b, 4c-d are displayed respectively B_θ , B_r and B_z vs. t in four different discharges (8 Torr of D_2, 11 kV). These B components have a peak amplitude with comparable values ($\sim 4 - 7.10^3$ G) in locations (see captions of Figs. 2,3,4) which can be explored with the probe but B_r and B_z may have different signs in different discharges (Fig. 4 c,d). This is consistent with the formation of current loops with one side of the loop on the axial column surface and extending far

off the discharge axis with a random location on z (see Fig. 5a). It has been verified that the B_z, B_r signals are not caused by a probe incorrect orientation; the signals from more than 100 discharges have been analyzed. The loop angular width about the electrode axis* can be quite small (e.g. $\lesssim 10^0$) for the loops stretching far from the electrode axis (> 1-2 cm by probe signals) and for the loops fitting the luminous pattern between cusps near the axis (the density drop prevents optical observation far from the axis). B_θ signals become larger than for the other components by moving the probe closer to the electrode axis ($\gtrsim 5 \times 10^4$ G at r > 10 mm from the axis; the probe is destroyed at a smaller distance from the axis).

An independent method to observe a close loop near the z axis is given by x-ray photographs (pinhole cameras, Be filters, 2 - 5 keV x-rays). In Fig. 6a is reported the image from a 18 kV discharge and in Fig. 6b the isodensity plots from one of the three sources in Fig. 6a. A circular loop with a sharp boundary (intensity relatively small at the center of the loop) is clear in Fig. 6b. The smoothing due to the microdensitometer aperture (75 μm) and the choice of the density steps give an apparent diameter of the loop ($\sim$ 50 μm) somewhat different than the actual loop diameter (the smallest we recorded). The flashing time (about 10 ns by collimated scintillation-detectors NE-102 and PU) of the x-ray source is short enough for considering time-integration effects not as a cause of distortions in the recorded image as compared with an image resulting by a shorter time of exposure.

*A loop is on or near a plane which contains the electrode axis; the angular width of the loop indicates how wide the loop extension is off this plane.

3. Ion Beams

The observation of ion beams in the forward direction is usually made in our experiment via ion-induced damage on targets of different materials.[10] The activation method of carbon targets[11] via $C^{12}(d,n)N^{13}$ is usually not effective to measure the fluence of deuteron with energy $\gtrsim$ 330 keV by operating our system with $\sim$ 6-7 kJ (at 16 - 18 kV). The ion beam intensity is usually too weak(†); only discharges with a neutron yield $n > \gtrsim 3\,\bar{n}$ at 5 Torr ($\bar{n} \cong 2 \times 10^8$ is the mean value of neutrons per discharge) clearly indicates that activation occurs.

Ion beams in the opposite direction (toward the anode) are not expected to be more intense than in the forward direction; acceleration of ions toward the anode may occur to match a fast increase of B_θ e.g. in a region where the column diameter is suddenly decreasing (necking).

We have used polystyrene foils (usually a stack of two or more foils, each 120 μm thick) and lucite plates as convenient targets in the forward direction, 36 cm from the anode end, and in the rear (at the end of the drift chamber of the electron beams; the target is at 50 cm from the forward end of the anode; larger or smaller distances have also been used). Our targets can discriminate - by a convenient mode of operation - between ions ejected from the focus region in the rear direction and ions which are collectively accelerated by the electron beams (the propagation speed of the beam is 75% of the speed of light). Damage caused by ions from the focus is reported in

---

(†) The counts of N^{13} β^+ decays in our case usually merge with the background unless a γ-coincidence system is used.

Fig. 7. The pitting is due to clusters of ions with energy of the order of 300 - 400 keV. The energy is obtained by comparison with damage (depth and shape) on metal plates[10] by similar conditions. This pitting (density of pitting) is reduced by about a factor 10 in the rear (180^{o}) target as compared with the front direction target and is apparently missing in some of the 180^{o} targets. Two apertures of the anode have been used (fully open anode or, alternatively, on a circular aperture of 4 mm at the center of the anode) see Fig. 6b. The pitting density at 180^{o} is not substantially modified by using the 4 mm aperture as compared with an exposure by fully-open anode. This indicates that the 180^{o} ions are emitted near the axis and at a small angle from the axis. The method for discriminating the electron-beam-accelerated ions is based on the identification of their typical damage pattern which has a very characteristic and regular geometry with a fine structure down to linear dimensions of 1 to 30 μm. The complete (elaborate) method for discriminating one group of accelerated ions from the other group is presented elsewhere.

A different type of target material (CR-39) has also been used at 0^{o} to determine (with a high resolution in space) the angular distributions of the ions with an energy above a chosen value. This is accomplished by covering the target with mylar foils as filters and by etching with NaOH the particle tracks. By observing tracks of deuterons with energy above 2.4 MeV (50 μm mylar filter) a deuteron density on the target up to $\sim 5 \times 10^{6}$ deuterons/cm^{2} is recorded. An important findingis the shape and extension of the area with this high density of tracks. In one discharge the reported value of ion density was uniform on an arc $\sim$ 3-4 mm wide, $\sim$ 2-3 cm long, with very sharply defined

boundaries (a drop of one order of magnitude of the track density is observed over a distance of 0.1 - 0.2 m on both sides of the arc).

The arc is centered on the axis of the discharge at about 2 cm from this axis. Arc location and geometry indicate that the source of these high energy ions can be the bubble that disrupts the off-axis part of the current sheath at $t \tilde{\sim}$ 200-250 ns. No measurements of this kind (by track etching) have been completed at 180°. In the rear direction a maximum of energy deposition has been observed by the maximum of electron beam damage. The energy deposition/cm^2 was estimated by the amount of material removed within components of the fine structure damage. By the duration of the beam (1 - 10 ns) we confirm a power deposition level $\sim$ 0.1 TW/cm^2 as previously reported.[6]

4. Conclusion

The formation of the current pattern outlined by $i_a(\rightarrow)$, $i_p(\rightarrow)$ in Fig. 5a is strongly suggested by beam intensity and emission sequence. The axial current i_a on the column and on the current sheath also at earlier stages is carried mainly by electrons in agreement with previous determination.[12] The current i_c in the central region of the loop is carried by ion and is enhanced by necking processes or by any process which increases the peak value of B_θ near the axis. The low density current i_p in the peripheral part of a loop is increased to peak values at a later time when the breakdown of current channels occurs in the axial column region after t = 0 ($|dI/dt|$ peak). The current pattern of the loop diverts current from anode-cathode circuit

and contributes to the decrease of I as the |dI/dt| peak is approached. This sequence is well fitting the observations of B_θ by magnetic probes which are located at different values of r near the anode face.[13] These observations indicate that B_θ is steadily increasing in regions with $r \geq 11.5$ cm up to the time at which the total current on the electrodes reaches the maximum value (t=0).[13] This finding is in agreement with values of $|i_c|$ large enough so that a decrease in $|i_c|$ is sufficient to offset the consequence of a decreasing value of i_a (and of I). It is interesting to note that other types of current loops can contribute to keep low the total magnetic energy while the field intensity increases in a localized region. One of these loops is outlined in the lower side of the cusped column in Fig. 5a (one side of the loop is forming a segment of the column wall). The column by this type of self-crowbarring process can decrease the field intensity on regions at a large distance from the axis while the field can increase inside the small diameter loop. It is inside those small diameter loops that our x-ray data analysis indicate > 10^8 G fields. A convenient use of these extreme field intensities would be to affect their time of decay for producing ion and electron beams for specific applications by exploiting their remarkable collimation and their high power level.

References

1. M. J. Forrest, B. A. Norton, N. J. Peacock. Proc. 6th European Conf. Plasma Phys. and Nuclear Fusion, Moscow 1973, J.I.N. Res. edit., vol. I, p. 363.
2. W. H. Bostick, V. Nardi, W. Prior, F. Rodriguez-Trelles. Proc. II Topic Conf. Pulsed High-Plasmas, Garching 1972, Lotz edit., p. 155.
   W. H. Bostick, V. Nardi, W. Prior. Annals New York Acad. of Sci. 251 (1975) 2.
   V. Nardi et al. High Magnetic Field Conference, Grenoble 1974 (CNRS ed.) p.129.
3. W. H. Bostick et al. in Energy Storage Compression and Switching, Plenum, New York, p. 255, 1975.
4. C. Patou, A. Simonnet, J. P. Watteau. Phys. Lett. 29A, 1, 1969.
   W. H. Bostick, V. Nardi, W. Prior, Plasma physics and controlled nuclear fusion research, Tokyo 1974 (IAEA, Vienna) Vol. 3, p. 109; Proc. 7th Europ. Conf. on Controlled fusion and plasma physics, Lausanne, 1975, Vol. 1, p. 62.
5. W. H. Bostick, V. Nardi, W. Prior, C. Cortese, Proc. 1976 Fusion Conference IAEA, Vienna.
6. W. H. Bostick, V. Nardi, W. Prior, C. Cortese, Proc. 1978 Fusion Conference IAEA, Vienna.
7. W. H. Bostick, V. Nardi, W. Prior, Proc. Thermophys. Conf., Newton, Mass. 1970, New York, 1971.
8. N. J. Peacock et al. Proc. 1971 Fusion Conference, IAEA, Vienna.
   The best time-resolved report of this process is given in the shadowgram sequence in this paper.
9. W.H.Bostick, V.Nardi,W.Prior, J.Plasma Physics, 1972,8,p.7 .

10. W. H. Bostick, V. Nardi, W. Prior, Journal of Nuclear Materials 63 (1976) 356-372.

11. R. L. Gullickson and H. L. Sahlin, Lawrence Livermore Laboratory Preprint UCRL - 77173, December, 1975.

R. L. Gullickson, J. S. Luce and H. L. Sahlin, Lawrence Livermore Laboratory Preprint UCRL - 78669, May 1976.

12. WH Bostick et al. same as ref.7; also Proc.Ionized Gas Confer., Oxford II 1971.

13. A. Bernard et al. Proc. 1978 Fusion Conference, IAEA, Vienna.

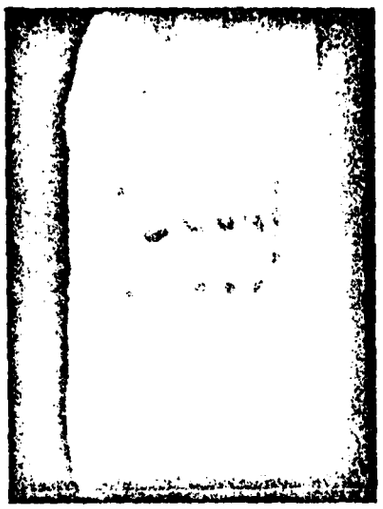

a

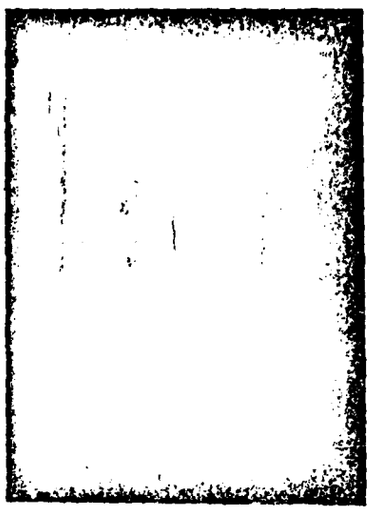

c

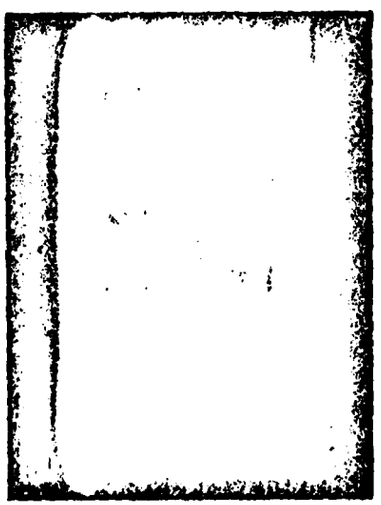

b

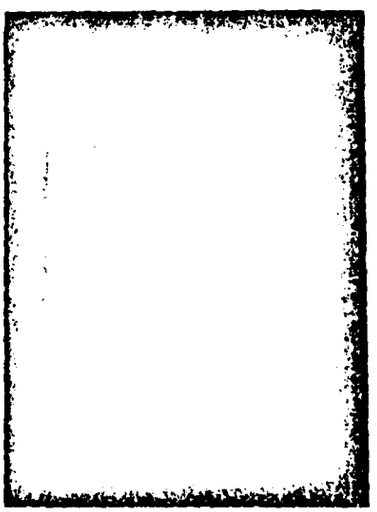

d

Fig. 1

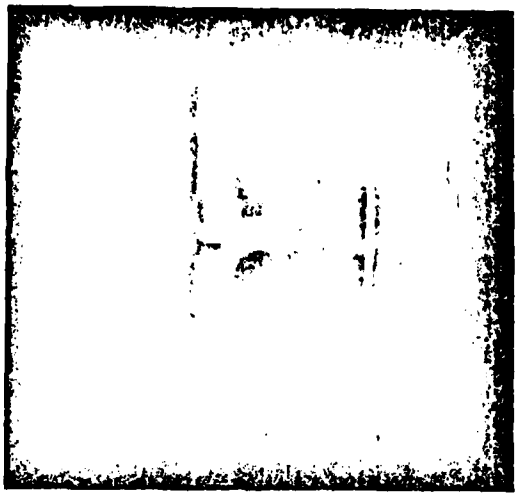

a

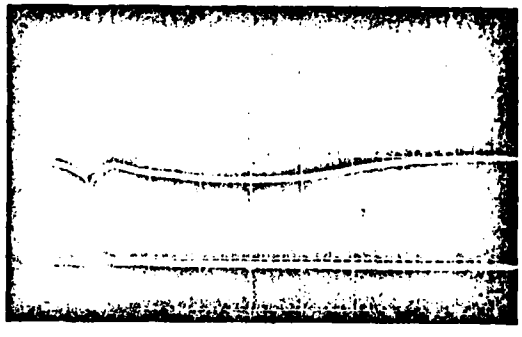

time-marking signal for photograph

b

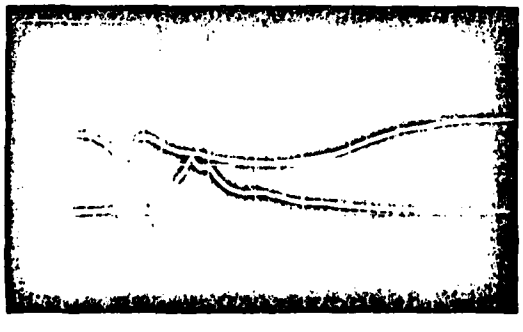

c

Fig. 2

a

b

Fig. 3

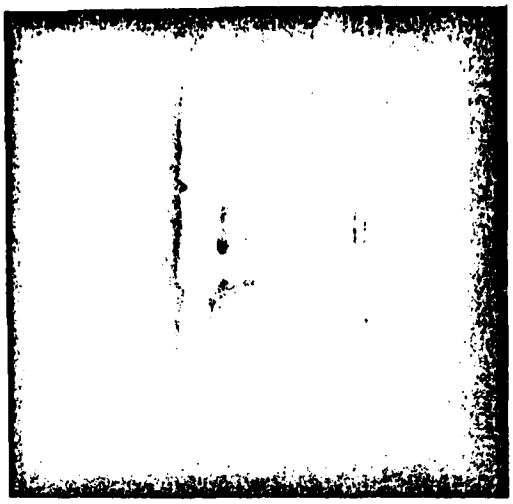

a

b

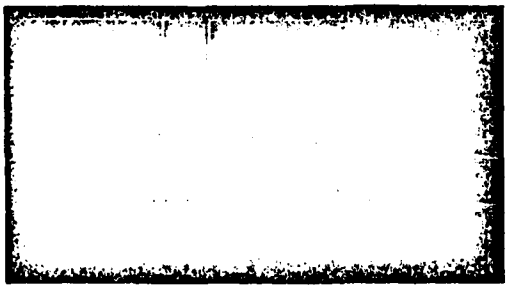

j
B_z

c

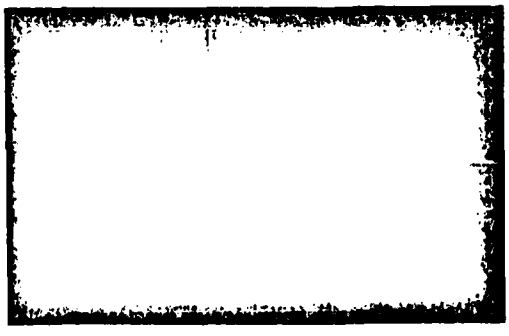

j
B_z

d

Fig. 4

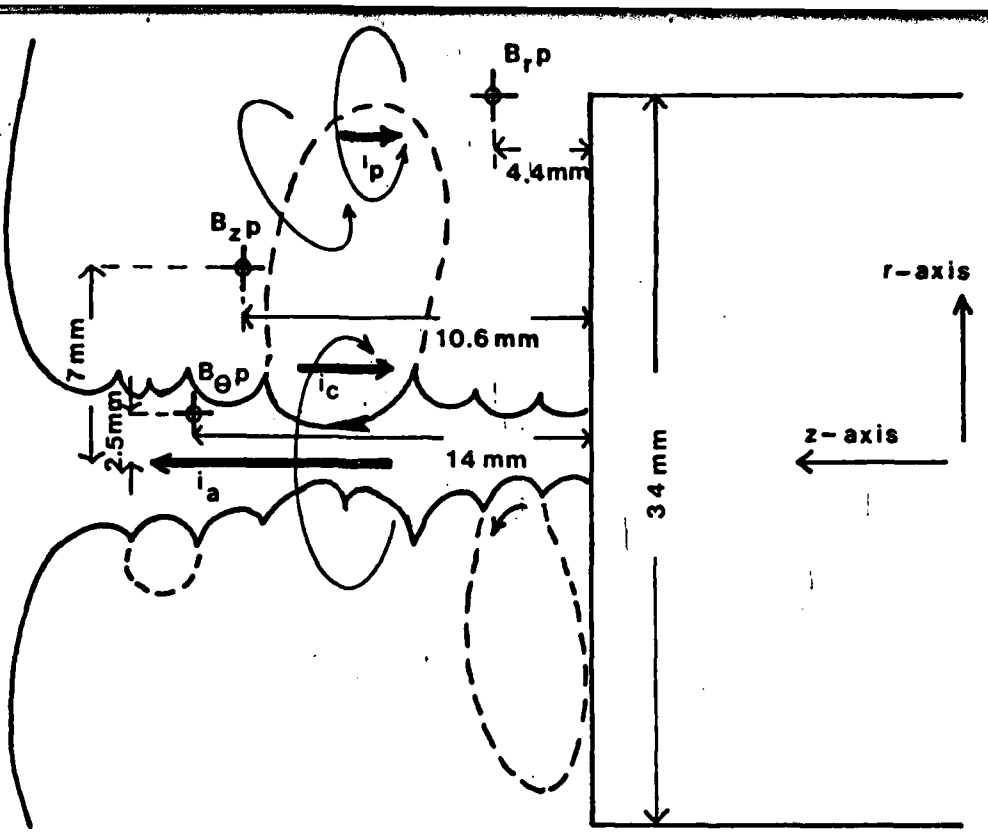
B_{rp}
4.4mm
i_p
B_{zp}
7mm
10.6mm
$B_{\theta p}$
i_c
2.5mm
14 mm
i_a
34 mm
r-axis
z-axis

a

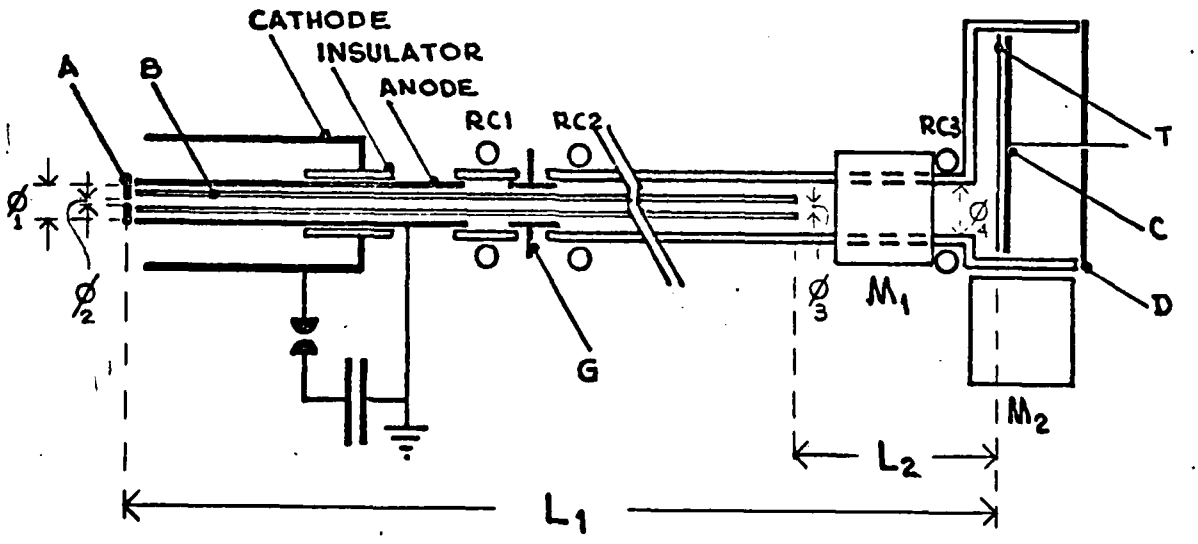
CATHODE
INSULATOR
ANODE
A
B
RC1
RC2
RC3
T
C
D
G
M_1
M_2
ϕ_1
ϕ_2
ϕ_3
ϕ_4
L_1
L_2

b

Fig. 5

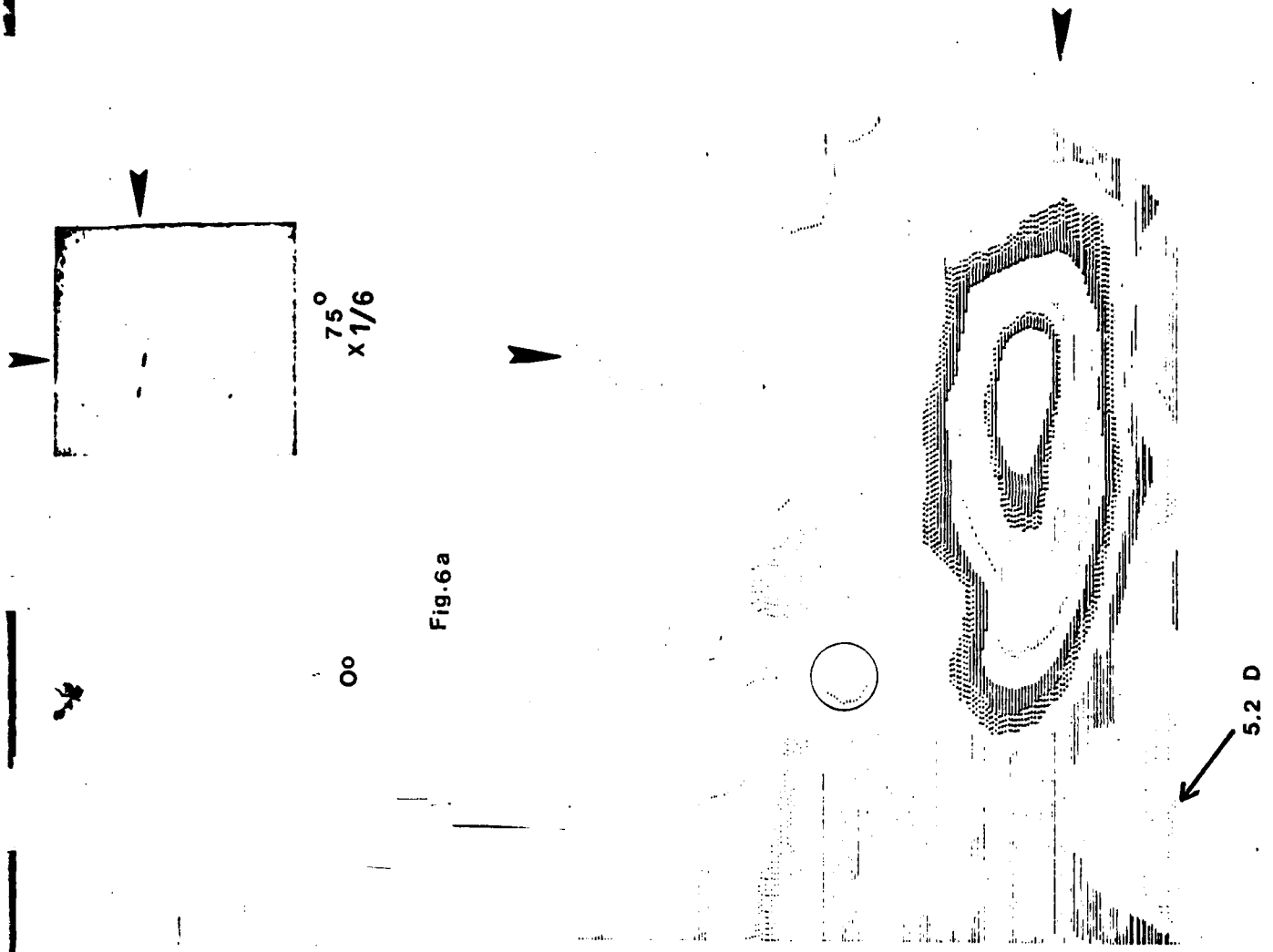

Fig.6a

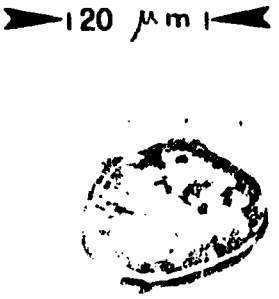

Fig. 7

Captions

Fig. 1 . a,b,c,d : Image-converter photographs of the plasma-focus axial column by visible light, 5 ns exposure, at the time of maximum compression (t=0). Note cusps and necking of the column (typical diameter of column = 4 mm; profile of anode diameter,3.4 cm, at right).

Fig. 2 . a : Same as Fig.1 but with magnetic probe . b : dI/dt trace (sweep speed 100 ns/cm) and (lower trace) time marking of photograph exposure. c : dI/dt signal and (below) signal of B_θ probe.

Fig. 3 . a : Same as Fig. 2 a. b : dI/dt signal and (below) B_r signal.

Fig. 4 . a, b : Same as Fig.2 a. c , d : dI/dt signals(above) and below B_z signals .

Fig.5 . a : Schematic profile of axial plasma column and current loop pattern fitting probe signals. b : Schematic of plasma focus electrodes and drift chamber for electron beam.

Fig. 6. a : X-ray pinhole photographs of axial plasma column (from 0° direction, magnification x6, and from 75° magn.x1; 3 keV x-rays). b : Microdensitometer plot of right part of 75° photograph as it is indicated by arrows. Circle at upper left marks loop region. Different plot markings indicate different steps of film density D.

Fig. 7 . Typical ion damage on a plastic target in the 180° direction (same direction of electron beam; target at 50 cm from source) . The electron damage can be easily differentiated from the ion damage.

IAEA-CN-37/U-3-3

ENERGY SPECTRA OF DEUTERON AND ELECTRON BEAMS FROM FOCUSED DISCHARGES AND OPTIMIZATION CRITERIA*

V. NARDI [§], W.H. BOSTICK [§], J. FEUGEAS [§], W. PRIOR [§+], C. CORTESE [+]

[+] Istituto Elettrotecnico Nazionale
Galileo Ferraris,
Turin, Italy

[§] Stevens Institute of Technology,
Hoboken, New Jersey,
United States of America

Abstract

ENERGY SPECTRA OF DEUTERON AND ELECTRON BEAMS FROM FOCUSED DISCHARGES AND OPTIMIZATION CRITERIA.

Deuteron beams ($\approx 10^5$ A) with a 300-keV peaked spectrum and electron beams are produced by localized sources (≈ 10 ns, ≈ 1 mm) in focused discharges. The energy spectrum of the deuteron beam ejected from a localized source in plasma focus discharges (45-75 μF at 15–18 kV; $I_{max} \sim 0.5 - 0.8$ MA) is derived by two independent methods: (A) ion time of flight and (B) ion-induced damage on Al plates. The ion spectrum varies from shot to shot but specific features are observed by all discharges. From method (A) the number of deuterons N(E) as a function of the ion energy E has a well defined maximum N_m 130 keV $\leqslant E \leqslant$ 320 keV. N(E) has a minimum at lower values of E and rises sharply again by further decreasing E. N(E) for $E \lesssim 50$ keV becomes substantially larger than N_m. The distribution of ion penetration range in Al yields by method (B) substantially the same spectrum as method (A). A second peak with maximum value N_M of N(E) for 15 keV $\lesssim E \leqslant$ 40 keV is derived by method (B), which is most convenient for deriving the low-energy tail of the ion spectrum ($N_M \sim 9\ N_m$). The electron-beam energy (with a dominant value $\approx$ 300 keV) is determined by the length of dendrites ($\approx$ penetration range) in a lucite target inserted inside the hollow-centre electrode (anode). The higher the maximum value E_M of the observed ion energy, the higher is the total neutron yield n in a discharge. By comparing two low-voltage discharges, higher values of E_M and n are observed in the discharge which generates fewer ion (and electron) beams. In a high-voltage discharge, n has instead higher values when the discharge generates many ion/electron beams. Generalized criteria for the optimization (maximum n) of a plasma focus are derived in terms of the propagation speed of the current sheath between electrodes and of conditions for avoiding restrike behind the current sheath first formed.

* Work supported in part by Consiglio Nazionale delle Ricerche, Italy; AFOSR, Washington, DC, AES, Inc., New York, New Jersey Power & Light Co., and Jersey Central Power & Light Co., USA.

J. Feugeas is on leave from Universidad Nacional de Rosario, Argentina.

1. INTRODUCTION

Low-cost sources of high-intensity ion beams are obtained by plasma focus discharges. In our case the discharge is fed by a 45-μF capacitor bank at 15 kV with 3–5 torr deuterium fillings. Electron beams are also produced in these discharges. The typical electron energy ($\approx$ 300 keV) is assessed by the length of dendrites on a lucite disc located inside the hollow-centre electrode (anode). The ion spectrum is determined by the ion penetration range in Al targets and by the ion time of flight from a localized source. We have obtained substantially coincident spectra by these two independent methods. The time-of-flight method in a D_2 discharge is simplified by using the D-D neutron emission. The bulk of the neutron emission in a discharge, i.e. a fraction $\gtrsim 50-70\%$ of the total neutron yield (10^8-10^9/shot), is produced in the hot plasma on the discharge axis by high-energy deuteron beams with a directed kinetic energy $\gtrsim$ 10 keV–1 MeV. Ion acceleration to peak energy and peak of the neutron pulse occur within a time interval $\lesssim 1-10$ ns. The neutron source – and so the corresponding source of high-energy ions – is formed in the hot plasma by one or (in some discharges) 2–10 localized regions of high density ($\approx 10^{20}$ cm^{-3}), each with linear dimensions < 1 cm. Each neutron pulse also has a tail $\approx$ 100 ns long which is produced by the part of the ion beam crossing the cold plasma. This non-localized part of the neutron source has an amplitude A_t neutrons ns^{-1} smaller by about 1/30 than the amplitude A_p of the neutron source main pulse (i.e. of the core of the neutron source). Pulse multiplicity/duration ($< 5-10$ ns) of the localized neutron sources in the hot plasma axial region fits multiplicity and duration of the hard (> 30 keV) X-ray pulses from the same plasma region [1]. It is consistent with collimated neutron measurements [2] and with X-ray pinhole-camera photographs [1, 3] to consider a localization in space of a neutron source (source core) even greater than the space resolution ($\approx$ 1 cm) of the neutron collimator, e.g. with the same linear dimensions[1] $\delta \approx 0.1-1$ mm of a localized X ray source [1]. A localization of a neutron (and ion) source in space within 1 cm and in time, as we have observed in our experiments [2], makes it possible to determine the energy spectrum of the ions by a time-of-flight method. The spectrum was derived for different plasma focus discharges by a time-of-flight method and by a method based on the distribution of the observed ion-penetration range in the Al plate.

[1] Note that the symbols δ, d in Sections 1 and 2 do not indicate the same quantities as in Sections 3, 4 and 5.

2. ION ENERGY SPECTRUM

(A) Time-of-flight method

The ion spectrum is derived by the ion time of flight from the localized source (±0.5 cm from centre of anode end) to an observation region located at a distance d = 10 cm downstream along the electrode axis. A paraffin collimator (gap width 1.5 cm) for neutron-collimated measurements is pointed at the region of observation (direction 90° from the electrode axis; distance of detector from axis $\Lambda = 76$ cm [2]. The time marks are given by the hard X-ray burst ($\cong 1-2$ ns duration) which is radiated simultaneously with (at time of production of) the ion beam (specfically at the time of highest increase in ion-beam intensity at the source and of neutron emission intensity). The neutron emission from the observed region (1.5 cm wide in the axial direction) rises sharply when the bulk of the beam front reaches this region (the field of view of the collimator). To derive the ion spectrum, we used a discharge in which only one strong localized source of neutrons and of hard X-rays is formed in the plasma; both pulses in the detector signal have a sharply defined onset time. Pilot U detector systems are used for both X-rays and neutrons; time resolution is $\approx 2-3$ ns. The emission duration τ of the ion source (and of the neutron source core) is determined by the duration of the hard X-ray pulse. The onset time of both ion and X-ray source is taken as t = 0. The time of flight Δt of the ions from source to collimator field of view (with its centre at distance d from the source) is estimated by disentangling both instrumental broadening of the pulse and deformation due to ion velocity spread (by ion beam propagating through d) from the pulse natural width due to the duration of emission. This is accomplished by a normalization of the X-ray signal amplitude $\dot{x}(t)$ to the neutron signal $\dot{n}(t)$ so that peak amplitude of the normalized X-ray signal and of the neutron signal have the same numerical value [$\dot{x}(t) \rightarrow \dot{x}_n(t) \equiv \dot{x}\,\mathrm{Max}\,\dot{n}/\mathrm{Max}\,\dot{x}$].

We then determine the time of flight $\Delta t(E)$ of the ions via the equation:

$$\dot{x}_n(t) = \dot{n}(t + \Delta t + \Lambda/v_n - \Lambda_s/c) \tag{1}$$

by detector outputs; $c = 30\ \mathrm{cm \cdot ns^{-1}}$; v_n is the neutron speed and Λ_s is the distance between X-ray (and ion) source and Pilot U detector ($\Lambda_s \approx \Lambda$). The number of ions $N_D \Delta E$ with an energy between E and $E + \Delta E$ is estimated by the equation:

$$N_D \approx \dot{n}/\sigma_{DD}(E) \tag{2}$$

where σ_{DD} is the cross-section for $D(D,n)^3He$ reactions; $E = \frac{1}{2} m_D (d/\Delta t)^2$. This approximate estimate of N_D is valid when $\delta/d \ll 1$, $d/\sqrt{(2E/m_D)} \gg \tau$; otherwise

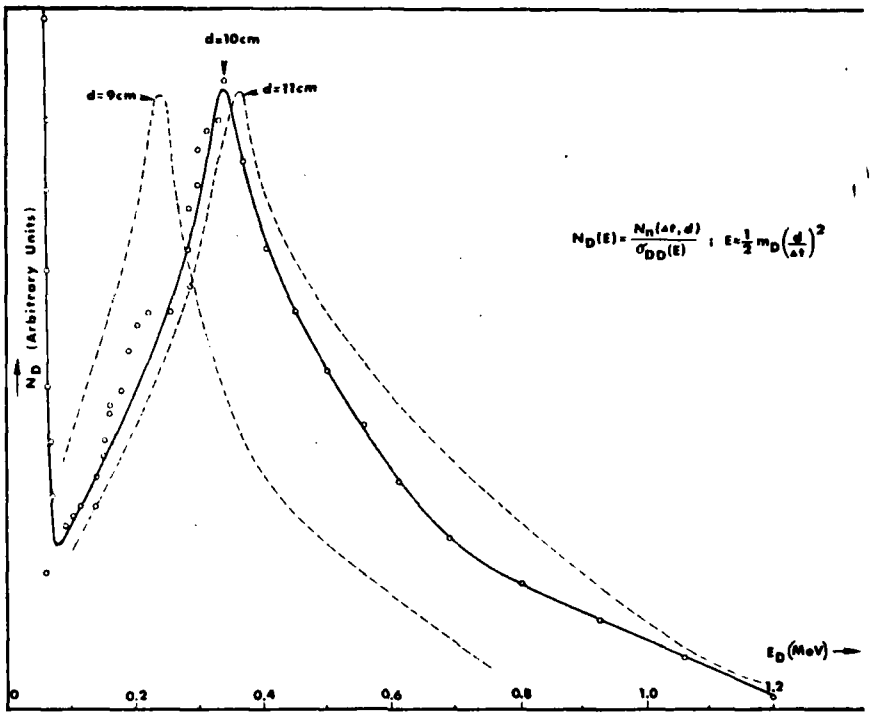

FIG. 1. Ion energy spectrum by time-of-flight method.

a more complicated integral equation involving a convolution integral over τ must be used instead of Eqs (1) and (2). The spectrum in Fig.1 is derived by Eqs (1) and (2) from a discharge with a sharp neutron and X-ray pulse (FWHM of the x pulse $\lesssim$ 3 ns; total neutron yield $n \sim 2 \times 10^8$). An alternative arrangement was also used with one of the two neutron-detector systems very close ($\approx$ 12 cm) to the localized source to monitor the intensity as a function of time without referring to the hard X-ray pulse. The consistency of all results has been verified. Energy losses of the ion beam in the relatively cold plasma have been considered and can be neglected for (A) energy values. The discharge chamber was filled with 3.4 torr of D_2. The assumption that the source of the ion beam is localized and coincides in space with the localized source of the first – sharply peaked – neutron and hard X-ray burst is critical in the derivation of the ion spectrum by this procedure. The dashed lines in Fig.1 give the deuteron spectrum for two different locations of the localized source of ions. A choice of values as d = 9 cm, d = 11 cm for the distance d between localized source and field of view of the collimator is still consistent with collimator-gap width.

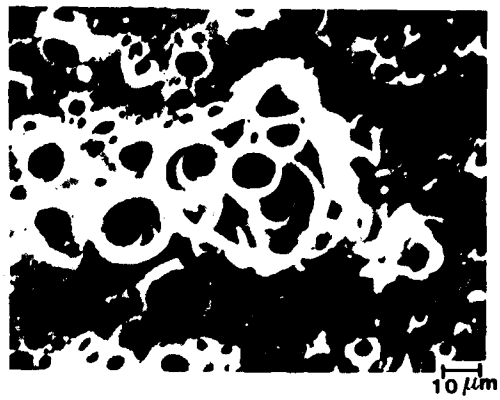

FIG.2. Scanning electron micrograph of Al plate used for deriving the spectrum in Fig.3. Exposure to a single discharge (by 5.6-torr D_2); neutron yield $\lesssim \frac{1}{2}$ yield of discharge generating spectrum of Fig.1.

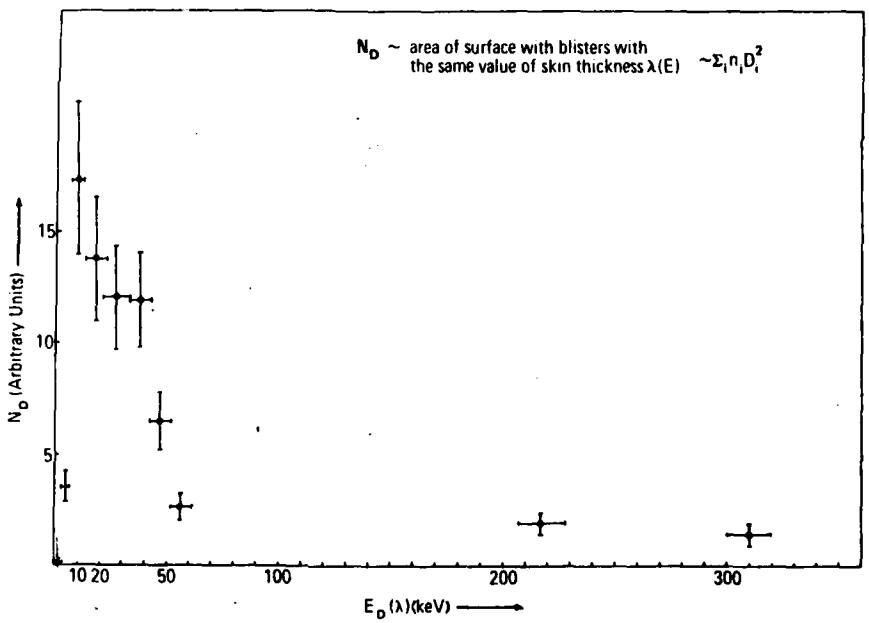

FIG.3. Ion spectrum from penetration range in Al plate [4].

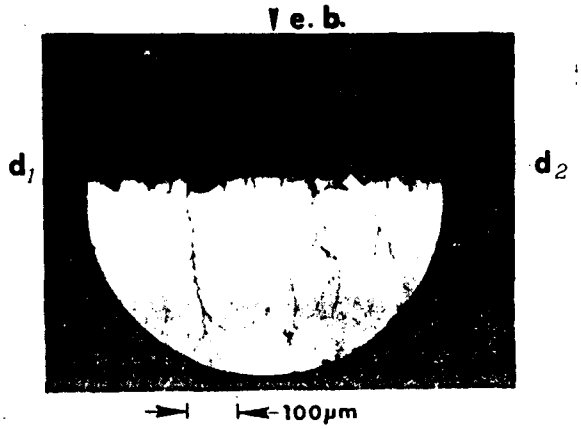

FIG. 4. Dendrites due to bombardment of electron beams with a directed kinetic energy orthogonal to the lucite surface d_1–d_2. The dendrite depth is determined by the electron penetration range [5]. The best-fitting value of the electron energy is ≈ 300 keV. The lucite is inserted inside the hollow-centre electrode ~ 10 cm from anode end. The surface of the plate (orthogonal to the electrode axis during exposure to a single discharge) is orthogonal to the plane of the photograph. (Photograph by optical microscope.)

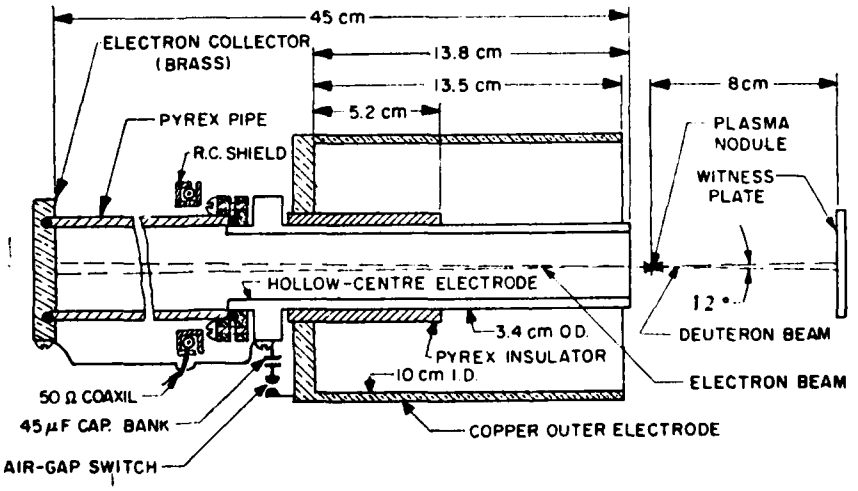

FIG. 5. Schematic view of plasma focus (PF) electrodes with drift chamber for the electron beam and the Rogowski coil (RC) arrangement on the left-hand side. A metal plate (Al) for observation of the ion-induced damage was located on the axial direction. The plate was exposed to a single shot; a shield protected the plate during preliminary discharges for electrode conditioning. Targets of plastic materials were located at the end of the drift chamber (45 cm from the beam source) or closer to the source.

(B) Radiation-damage method

The surface of an Al plate orthogonal to the discharge axis is located 9 cm from the anode end. The deuteron energy E is determined by the skin thickness of the blisters which are produced by ion bombardment of the plate. The skin thickness gives the projected range $\lambda(E)$ in Al. From the observed value of λ on a blister we derive the dominant energy E of the deuterons bombarding the plate at the location of the blister. The number of deuterons with a specific value of the energy E is considered to be proportional to the area covered by blisters with the same value of $\lambda(E)$. This area is proportional to $\Sigma_i n_i(E) D_i^2(E)$, where $D_i(E)$ is a specific value of the diameter of one (or many) blister(s) with skin thickness $\lambda = \lambda(E)$, and n_i is the number of the blisters with these values $D_i(E)$, $\lambda(E)$. The spectrum peak in Fig.1 is given by ions which generate the blisters with the largest observed value of $\lambda(E)$ as in the cluster of blisters at the centre of Fig.2. Multiple readings of $D_i(E)$ and $\lambda(E)$ have been made for all the blisters ($\gtrsim 2$–4×10^3) covering typical sample areas (each area $\approx 0.3 \times 0.5$ mm^2) of the Al plate. The ion spectrum is reported in Fig.3. The error bar is the standard deviation which is generated by using minimum and maximum value of D_i and of λ from the multiple readings on each blister. The ion beam propagates within a $\approx 12°$ cone on the electrode axis. The detailed internal structure of the beam is recorded by the Al plate damage (a tentative estimate of the ions with energy $\gtrsim 200$ keV gives $\gtrsim 10^{16}$; $\gtrsim 10^{12}$ ions with this energy are necessary to form one cluster of blisters as in Fig.2).

3. ENERGY AND TOTAL CHARGE OF ELECTRON BEAMS

A disc of Plexiglass (polymethylmethacrylate – PMMA) was used as a target for the electron beams which propagate along the anode axis (see Figs 4 and 5). The disc, ~5 mm thick, had the same diameter as the hollow-centre electrode (anode) and was fitted inside the anode at a distance > 10 cm from the anode end where electron beams are generated with a maximum of energy (disc surface orthogonal to the electrode axis). Dendrites are formed in the PMMA after exposure to a single plasma-focus discharge (see Fig.4) as a consequence of the fact that electrons are stopped and trapped within the PMMA and a negative space charge builds up. PMMA breakdown occurs after or during the electron bombardment. The dendrites form the discharge pattern inside the PMMA (Lichtenberg figures) and indicate that the PMMA is ruptured through the irradiated volume; the disc surface on the side of the plasma is at the positive voltage. The PMMA breakdown and the formation of the discharge pattern are easily understood by assuming that the bulk of the space charge in the PMMA is localized in a relatively thin layer parallel to the exposed – or free – surface of the disc which is

TABLE I. DATA FROM DENDRITES IN PMMA (A DISC LOCATED INSID CENTRE ELECTRODE-ANODE)

Q (charge of thin layer inside PMMA) = CV_{br}

V_{br} (breakdown strength of PMMA at 100°C) ~ 5 MV cm^{-1}

$C = \frac{\epsilon A}{\delta}$ capacitance of dielectric slab of thickness δ and area A

δ = observed distance between region from which dendrites originate and free surface of dielectric ($\epsilon = 2.5$ dielectric constant of PMMA)

($\delta \lesssim$ mean forward electron range in PMMA)

A = area of damaged dielectric surface ~ 0.1 cm^2 (depending on neutron yield)

Three typical values of δ have been observed (the PMMA disc is exposed to a single discharge)

$\delta(\mu m)$:	400 ± 5%	100 - 140	15–20
E_e(keV):	300	130–140	44–52
Q(Coulomb):	2.5×10^{-4}	$10^{-3} - 7 \times 10^{-4}$	$6.5 \times 10^{-3} - 2 \times 10^{-}$

bombarded by the electron beam. Experiments by other laboratories provide evidence of the high concentration of the space charge in a narrow layer in PMMA samples which had been irradiated by a monochromatic electron beam [6].

The distance δ between the charge layer and the free surface of the disc is given by the depth of the sharply defined region from which the dendrites originate.

An estimate of the energy E_e of the bulk of the electrons in the beam is immediately obtained by taking the electron penetration range $\lambda_e(E_e) \cong \delta$ (E_e versus λ_e is taken from Ref.[7]). The true value of the electron energy is somewhat larger than the value of E_e as derived by this method because of the retarding field created by the charge build-up in PMMA; the relative importance of retarding field and of collision losses in slowing down the electrons has been determined experimentally by other laboratories [8]. Table I gives the three typica values of δ which have been observed in a PMMA sample after exposure to a single PF discharge. The short duration of the electron beam (~100 ns) ensures that charge-leakage effects before PMMA breakdown can be neglected.

One component of the electron beam for each observed value of δ can be defined by characterizing a beam component by the corresponding value of E_e. The voltage due to charge accumulation in one of the three PMMA layers becomes large enough for breakdown on a time interval which cannot be expected to be the same for the three observed values of δ. Our experimental data justify the assumptions that the localized sources of the electron beams coincide in space and

time with the localized sources of the X-ray emission and that both have similar variations with time.

From the variations of the X-ray emission [3] we can consistently assume that the deposition in PMMA of the high-energy component of the beam ($E_e \gtrsim 300$ keV (see Table 1)) is completed earlier and on a shorter time interval than for the other two components; the low-energy component (~ 50 keV) starts later and lasts longer than the other two components.

Under this assumption, the breakdown of the PMMA slab from free surface to $\delta \cong 400$ μm can be considered essentially independent of the breakdown processes of the two slabs with a smaller δ (these are considered to be mutually independent as well; non-interference among the three breakdown processes is also suggested by the observation that the dendrites have a tree-like pattern with few twigs and do not extend to the whole slab volume (see Fig.4)) [9]. In agreement with the previous assumption, we can estimate the electric charge Q which is deposited in each of the three thin layers inside the PMMA disc by using the formula for a planar capacitor with the dielectric breakdown strength of PMMA, i.e. $V_{br} \cong 5$ MV·cm^{-1} (an intrinsic breakdown mechanism is effective in our case) [10]. The estimated values of Q and E_e are shown in Table I.

4. ELECTRON BEAMS

A Pyrex pipe was attached at the back end of the centre electrode (Fig.5) to serve as a drift chamber for the electron beams. A shielded Rogowski coil (RC) encircling the Pyrex pipe was used to pick up the dI_e/dt signal due to electron beams. This RC was monitored simultaneously with the dI/dt signal from the total current on the electrodes. A second RC was used in many shots simultaneously with the first coil in order to obtain the integrated signal for I_e. The display of these signals from a Tektronix 7844 Oscilloscope is shown in Fig.6.

The two RCs which give the signals in Fig.6(a,b) are ≈ 20 cm away from the localized source of the electron beam (the coil location was changed in some discharges). A variety of tests were made to check the noise level and the possibility of spurious signals and to verify that the RC signal is indeed generated by the electron beam current I_e. In one type of test, (A), the shielded RC was lifted at the side of the drift tube and the display sensitivity increased several times. No signal was detected in this case. In another type of test, (B), the end of the anode near the focus was closed by a metal disc. Also, in this case the signal from the shielded RC, as in Fig.5, was absolutely flat. This and the observed damage (a circular spot with area ≈ 0.1 cm^2) on a target at the end of the drift tube after a single shot prove that the RC signal is caused by the electron beam current I_e.

The rise of I_e to peak value is very fast and in some shots is about 10 ns. The maximum observed value of I_e over about 50 shots was ≈ 5 kA. It could be

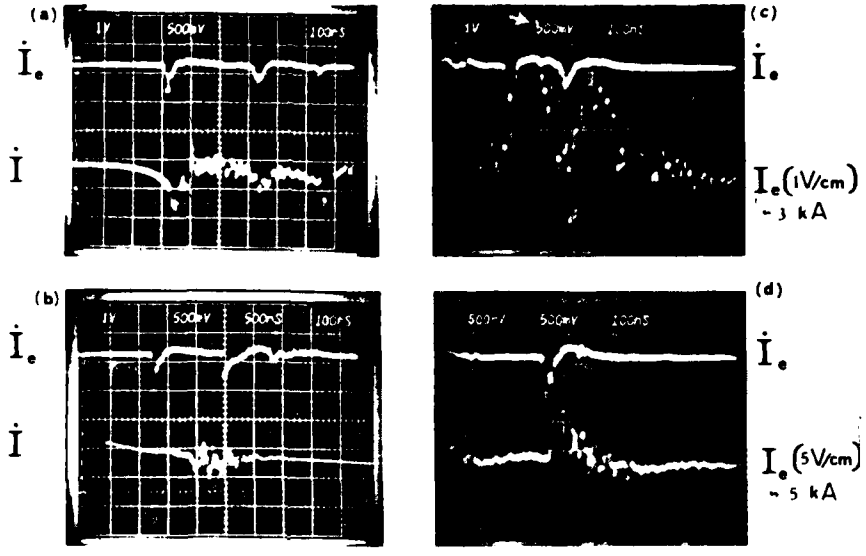

FIG. 6. Rogowski coil (RC) signals for direct measurement of the electron beam current I_e. The amplitude of the upper trace in (a), (b), (c) and (d) (12.5 $V \cdot cm^{-1}$, sweep speed 100 $ns \cdot cm^{-1}$, time increases from left to right) gives the time derivative $\dot{I}_e$ of the beam current. This signal comes from a shielded RC located as in Fig. 5 (coil length 66 mm, 23 turns with dia. of 2.2 mm). As a reference the lower trace in (a) and (b) (10 $V \cdot cm^{-1}$) gives the time derivative $\dot{I}$ of the electrode current I; sweep 100 $ns \cdot cm^{-1}$ in (a) as in upper trace; 500 $ns \cdot cm^{-1}$ in (b). The lower trace in (c and (d) gives I_e from a self-integrating RC which is located near the first coil in the same discharge. The RC for I_e (a calibrated coil of Physics Int. Co., 2.43 $V \cdot kA^{-1}$) was unshielded to evaluate the noise level. A numerical integration of $\dot{I}_e$ was always made to check that the measured value of I_e was the same (within 10% or better) for both RCs. The discharge in (a) was produced with a D_2 filling at 6 torr (neutron yield $n = 2 \times 10^5 \simeq \bar{n}$; in (b), (c) and (d), 7 torr of H_2). One electron beam was usually observed for each sharp $|\dot{I}|$ peak. The first peak in $\dot{I}_e$ (not recorded) was used to trigger the oscilloscope (a Tektronix 7844) in (c) and (d).

that the actual value of I_e is substantially higher, by a factor 10–40, than the RC value because of the return current which is carried by collectively accelerated ions from the gas (6 torr D_2, or H_2, as in the discharge chamber) and/or by the polarization current on the wall of the chamber. By using the value $I_e \approx 5$ kA for a beam of electrons of 300 keV with a cross-sectional area ≈ 0.1 cm^2, we estimate a power of 15 $GW \cdot cm^{-2}$ for this 15-J beam at the target. The hard X-ray signal from the beam-source region has a FWHM of 1–2 ns (scintillation detector signal). By taking this as the duration of the beam source, the power at the source is 0.15 $TW \cdot cm^{-2}$ or higher if the source diameter is smaller (this is certainly our case). A higher power value can be estimated by the energy deposition data

from the target which is consistent with a value of I_e as corrected for return current effects. Table I shows that the energy carried by a beam can be as high as ≈ 500 J, i.e. 10% of the energy of the capacitor bank. The power of the 300-keV component of the beam (≈ 100 J) which has the shortest duration at the RC distance from the source is then ≈ 0.1 TW · cm^{-2}, and near the source the power is then at least 1 TW · cm^{-2} or higher. These values coincide with the estimated power of the ion beam in the forward direction.

5. dI/dt DATA

For each peak (or for each group of partially unresolved peaks) spanning ~ 100 - 500 ns in the dI/dt signal (at the time of neutron emission onset) we have observed the emission of sharply collimated electron beams which propagate along the axis of the hollow anode. To find a possible correlation between total neutron yield, multiplicity of electron beams and the details of the dI/dt signal, we have analysed the dI/dt signals of ≅ 300 discharges with D_2 (6 torr) filling with a 75-μF capacitor bank at different voltage values (12.5 – 19.5 kV).

An external inductance was attached to this system (PF-2) in order to have for V ≅ 17.5 kV the same value of the peak current $I_0 \cong 7 \times 10^5$ A on the electrodes as in the 45-μF system (PF-1) at 16 kV that was used for the electron beam experiment reported in Section 4. The modified inductance of capacitor bank, transmission line and electrodes of PF-2 was $L_0 \cong 60$ nH, i.e. 1.5 times the original value of L_0 *(40 nH) for usual PF-2 operation. Figure 7 shows the mean value* $\bar{n}$ of the neutron yield (n = neutrons/shot) over N shots with a specific value of the voltage V on the electrodes for seven different values of V (N ≅ 40 shots for each value of V; the error bar in $\bar{n}$ is $\sigma/(N-1)^{\frac{1}{2}}$; σ = standard deviation).

The occurrence of restrikes on the electrodes is affected by the value of L_0. The purpose of these measurements was also to find the influence of restrikes behind the first current sheath on the axial-focus stage of this first sheath. The analysis of our data indicates that:

The correlation coefficient α_1 for n versus ν (ν = number of sharp peaks in the $|\dot{I}|$ signal from one discharge $\nu \cong 1-10$) is negative ($\alpha_1 = -0.45$) for low-voltage discharges ($V \leqslant 14$ kV; number of discharges, about 50). The probability of non-significant random effects as a cause of this value of α_1 is < 0.1.

$\alpha_1 \cong 0$ (no correlation) for intermediate voltages ($15 \leqslant V < 17$ kV).

$\alpha_1 \cong 0.4$ (positive correlation) for a higher voltage ($V \geqslant 18$ kV).

Similar behaviour was observed in the correlation coefficients for n versus ΣH_i, n versus ΣH_i^2, η versus $\Sigma H_i \Delta_i$, where H_i is the maximum value of the

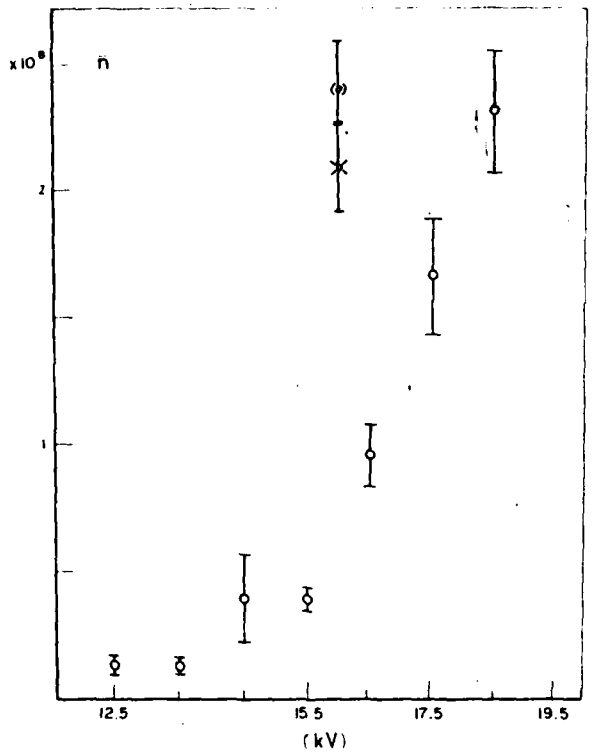

FIG. 7. The data points ○ give the mean value $\bar{n}$ of the neutron yield versus voltage for a 75-μF plasma focus with $L_0 = 60$ nH, (○) for the same system but a smaller external inductance ($L_0 \approx 40$ nH) and ⋊ for a smaller (45-μF) plasma focus. Electrode and insulator geometry is identical in all cases; the filling pressure, 6 torr of D_2 in all cases, is the observed optimum pressure (maximum neutron yield) for the 45-μF plasma focus at 16 kV.

i^{th} peak in $|\dot{I}|$, and Δ_i is the FWHM of this peak. For all discharges at 17.5 kV, a more detailed analysis was carried out. The steepness of the rise of the $|\dot{I}|$ signal versus time was evaluated for the first peak of $|\dot{I}|$ in a time interval from 150 ns before the $|\dot{I}|$ peak to peak time $t = 0$. $|\dot{I}|$ was fitted with $A\bar{t}^{\gamma}$; $\bar{t} \equiv (t(\text{ns}) + 150)/150$. The value of γ fitting best between 50 and 10 ns before the peak was derived for a group of high-yield discharges, $n = 3\ \bar{n}$, with a mean value $\bar{\gamma} = 4.5$, and for the group of all the other discharges ($0.1\ \bar{n} < n \leq 1.5\ \bar{n}$) with a mean value $\bar{\gamma} = 3.9$. This result is considered significant. The area ΔI_1 under the first $|\dot{I}|$ peak was also numerically estimated for these two groups of 17.5–kV discharges; ΔI_1 for the high-yield discharges (15% of all discharges at 17.5 kV) has the largest mean value; the ratio of the mean values of ΔI_1 of the two groups is = 8.5/6.5.

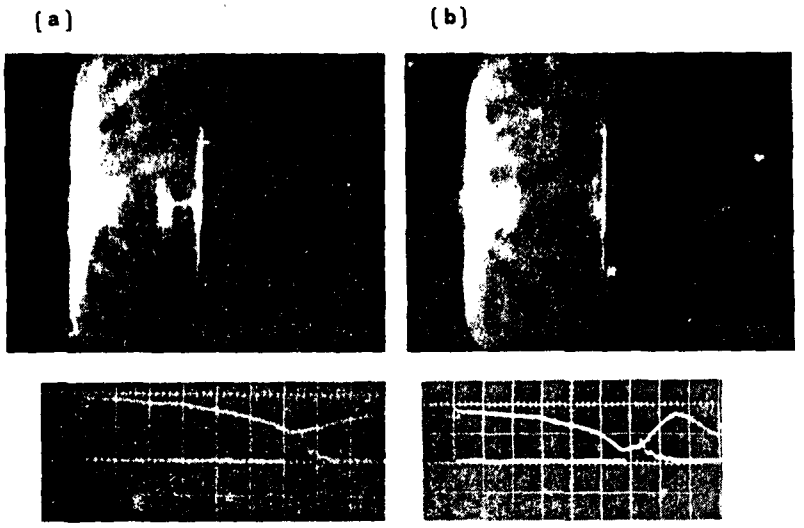

FIG.8. Image converter photograph by visible light (5 ns exposure).
Upper trace: dI/dt (I = electrode current, sweep 100 ns·cm^{-1}).
Lower trace indicates time at which photograph is taken (low-voltage discharge: 11 kV).
The picture (a) was taken at the time t_0 of $|dI/dt|$ peak, the picture (b) at a time t_0+100 ns.

Low-yield discharges have $\int I$ signals which frequently indicate the occurrence of restrikes at late times. A conclusion of these measurements is that in order to have a high-yield discharge at a relatively low voltage (and low speed of the current sheath) the production of a small number of electron beams corresponds to the optimization of the system. At a high voltage the reverse is true (the production of many beams seems to help avoid restrikes and to prevent the formation at a late time, ≈ 1 μs after the first discharge on the insulator, of another current sheath behind the first sheath.

Figure 8 shows images by visible light of two discharges at low voltage (45-μF system at 11 kV, 6 torr). Under these conditions the disruption of the current sheath is relatively slow, over a time interval $\geq$ 100 ns.

This provides a good opportunity to analyse the geometry of the axial pinch during the time of production of one electron beam. The time of production of the first electron beam coincides with the exposure time of the photograph in Fig.8(a). This indicates that the electron beam acceleration may occur in the disrupted region (dark area) of the axial column and it can be focussed in the neck of the pinch (different discharges usually have a different number of pinch neckings). The dark area can be considered as the gap of a plasma diode [11].

Figure 8(b), a different discharge, then shows that the 'electrode gap' distance (
of this plasma diode is increasing with time.

Child's law ($j = 2.34 \times 10^3 V^{3/2} d^{-2}$ ampère/cm^2) for a space-charge limited current can then be used to determine tentatively the electron current density j knowing V, d or the beam accelerating voltage V by J, d (the length scale in Fig. is given by the profile of the centre electrode of diameter 3.4 cm). Any attempt define a reliable effective parameter from this diode requires observations of a l number of discharges.

Child's law gives $V \lesssim 10$ volts for an observed value $d \approx 1$ mm (Fig.8) and a electron beam current $I_e < 10^5$ A ($Q < 10^{-3}$ Coulomb, from Table I). An observ value $V \gtrsim 300$ kV may indicate that Child's law is not valid in the electron-beam generating region and/or that the actual electron beam diameter is much smaller ($< 5-10$ μm) than the electron-beam diameter estimate by time-integrated effec

6. CONCLUSION

We estimate that at least $\approx 10^{12}$ ions are needed to produce a cluster of blisters as in Fig.2. About 10^4 of such clusters are produced in a single discharg by an ion burst with a duration ≈ 10 ns. The corresponding ion current is then $\approx 10^5$ A. The high-energy tail ($> 1-5$ MeV) of the ion spectrum can be reveale by neutron energy analysis [12] and by ^{27}Al(d,p)^{28}Al and ^{63}Cu(d,2n)^{63}Zn, ^{65}Cu(d,2n)^{65}Zn reactions [13]. The ion spectrum varies from shot to shot but specific features are observed by all discharges. From method (A) the number o deuterons N(E) as a function of the ion energy E has a well defined maximum N for 130 keV $\leqslant E \leqslant$ 320 keV. N(E) has a minimum at lower values of E and rises sharply again by further decreasing E. N(E) for $E \lesssim 50$ keV becomes substantial larger than N_m. N ($E \sim 1$ MeV) can still be as high as ~ 0.1 N_m. The distributio of ion penetration range in Al yields by method (B) substantially the same spectrum as method (A). A second peak with maximum value N_M of N(E) for 15 keV $\lesssim E \leqslant 40$ keV is derived by method (B), which is most convenient for deriving the low-energy tail of the ion spectrum ($N_M \sim 9$ N_m). A peak at the sa energy ≈ 300 keV for both electron and ion spectra fits a particle acceleration process in which the same field accelerates both ions and electrons.

REFERENCES

[1] BOSTICK, W.H., et al., in Energy Storage, Compression, and Switching (Proc. Int. Conf. Turin, 1964),Plenum Press (1976) 261.

[2] BOSTICK, W.H., NARDI, V., PRIOR, W., Plasma Physics and Controlled Nuclear Fusion Research 1976 (Proc. 6th Int. Conf. Berchtesgaden, 1976) Vol.3, IAEA, Vienna (1977) 497.

[3] BOSTICK, W.H., NARDI, V., PRIOR, W., J. Plasma Phys. **8** (1972) 7.
[4] BOSTICK, W.H., et al., J. Nucl. Mater. **63** (1976) 356.
[5] SPENCER, L.V., Natl. Bureau of Standards, Monograph 1 (Sept. 1959);
MOLEN, G.M., Aerospace Corp. Rep. (8 Apr. 1976).
[6] GROSS, B., J. Polymer Sci. **27** (1958) 138.
[7] BERGER, M.J., SELTZER, S.M., Tables of Energy Losses and Ranges of Electrons and Positrons, US Dept. of Commerce, Rep. N65-12606 (1964).
[8] LACKNER, H., KOHLBERG, I., NABLO, S.V., J. Appl. Phys. **36** (1965) 6.
[9] FUJITA, J., HIRAOKA, E., OKAMOTO, S., J. Appl. Phys. **37** (1966) 1873.
[10] O'DWYER, J.J., Theory of Dielectric Breakdown of Solids, Oxford Univ. Press (1964) p.111.
[11] NARDI, V., in Proc. 2nd Topical Conf. on Pulsed High-Beta Plasmas, Garching, 1972, p. 163;
NARDI, V., BOSTICK, W.H., PRIOR, W., Coll. Int. CNRS No.242, Physique Champs Magnétiques Intenses, Grenoble, 1974 (PAUTHENET, R., Ed.), (1975) 129.
[12] BOSTICK, W.H., NARDI, V., PRIOR, W., Plasma Physics and Controlled Nuclear Fusion Research 1974 (Proc. 5th Int. Conf. Tokyo, 1974) Vol.3, IAEA, Vienna (1975) 109.
[13] GULLICKSON, R.L., SAHLIN, H.L., J. Appl. Phys. **49** (1978) 1099, and literature quoted therein.